Unique Appearance of Lamellar Cleavage Patterns on Fracture Surfaces of Ti-Based Amorphous Matrix Composite

CHANGWOO JEON, BYEONG-CHAN SUH, CHOONGNYUN PAUL KIM, HYOUNG SEOP KIM, NACK J. KIM, and SUNGHAK LEE

In order to improve mechanical properties of Ti-based amorphous matrix composites basically composed of ductile β-Ti dendrites and brittle amorphous matrix by overcoming their inherent brittle nature, their fracture mechanisms should be verified in relation with microstructure, stress intensity factor level, and crack growth rate. In this study, thus, detailed fractographic observations including the unique appearance of lamellar cleavage patterns, which has not been reported in previous studies on conventional metals and alloys, were conducted. According to fractographic results, lamellar cleavage patterns were formed by repeated interruptions of crack propagation on {100} cleavage planes by difference between dendrite orientation and loading direction. Ductile-to-brittle transition phenomenon (ductile dimpled fracture → lamellar cleavage fracture → ordinary cleavage fracture in dendrite areas, and vein pattern → smooth pattern in amorphous matrix areas) occurred with increasing crack growth rate was also plausibly explained by the concept of time required for crack growth as well as dendrite orientation.

DOI: 10.1007/s11661-015-2842-3

I. INTRODUCTION

RECENTLY, advances in bulk amorphous alloys have been remarkably made by developing amorphous alloys with high glass-forming ability,[1–7] but there are problems to be solved, typical one of which is brittle fracture.[8,9] In order to overcome this brittle fracture, development activities on composite-type alloys by homogeneously distributing ductile crystalline dendrites in Zr- or Ti-based amorphous matrix have been actively performed.[10–16]

In order to systematically understand and improve mechanical properties of these amorphous matrix composites, fracture mechanisms should be verified in relation with composite microstructures basically composed of ductile dendrites and brittle amorphous matrix.[17–19] A simple way widely used to investigate fracture mechanisms is a phenomenal observation of fractured surfaces, the results of which have been mathematically quantified to effectively describe mechanical properties. Studies on detailed fracture mechanisms such as direct observation of crack initiation and propagation processes[17–19] or deformed microstructures beneath fractured surfaces[19–22] have also been conducted. Lately, the scope of understanding of fracture mechanisms is extended as electron microscopes are more widely used.[23,24] In spite of these efforts, many difficulties still remain to be addressed to correlate microscopic fracture mechanisms with macroscopic mechanical properties and to systematically analyze and predict them. In many cases, microscopic fracture modes are occasionally varied with loading directions and modes of applied stresses or crack propagating rates,[25,26] and ductile-to-brittle transition phenomena can occur even in the same material or temperature,[27,28] but only limited information is available.

In the present study, therefore, fracture modes of a Ti-based amorphous matrix composite containing ductile dendrites and amorphous matrix were investigated in relation with stress intensity factor level and crack growth rate using an *in situ* loading stage installed inside a scanning electron microscope (SEM) chamber.[17–19] Detailed fractographic observations including unique appearance of lamellar cleavage patterns, which has not been reported in previous studies on conventional metals or alloys, were conducted. Ductile-to-brittle transition phenomenon occurred with increasing crack growth rate was also interpreted by the concept of time required for crack growth as well as dendrite orientation. These experimental results provide evidences for the formation of lamellar cleavage patterns, which is attributed to the repeated interruption of crack propagation on {100} cleavage planes by difference between dendrite orientation and loading direction.

CHANGWOO JEON, Postdoctoral Researcher, and CHOONGNYUN PAUL KIM, Research Professor, are with the Center for Advanced Aerospace Materials, Pohang University of Science and Technology, Pohang 790-784, Korea. BYEONG-CHAN SUH, Postdoctoral Research Associate, is with the Graduate Institute of Ferrous Technology, Pohang University of Science and Technology, Pohang 790-784, Korea. HYOUNG SEOP KIM and SUNGHAK LEE, Professors, are with the Center for Advanced Aerospace Materials, Pohang University of Science and Technology, and also with the Materials Science and Engineering, Pohang University of Science and Technology. Contact e-mail: shlee@postech.ac.kr NACK J. KIM, Professor, is with the Graduate Institute of Ferrous Technology, Pohang University of Science and Technology, and also with the Center for Advanced Aerospace Materials, Pohang University of Science and Technology.

Manuscript submitted October 18, 2014.
Article published online March 18, 2015

II. EXPERIMENTAL

A Ti-based amorphous composite whose chemical composition was $Ti_{53.9}Zr_{30}V_{9.9}Ni_{3.5}Al_{0.9}Be_{1.8}$ (at. pct) was used in this study.[29] The composite was fabricated by a vacuum arc melting method under an argon atmosphere, held at 1073 K to 1173 K (800 °C to 900 °C) for 30 minutes, and quenched to sufficiently obtain the amorphous matrix. The composite was polished in diamond pastes, etched by a solution of 40 mL HF, 20 mL HNO_3, 40 mL HCl, and 200 mL H_2O, and observed by an SEM (model; JSM-6330F, Jeol, Japan). Electron back-scatter diffraction (EBSD) analysis was conducted by a field emission scanning electron microscope (FE-SEM, model; Helios Nanolab™, FEI, USA). The composite was machined into plate-type tensile specimens of 2.5 × 6.4 × 1 mm in the gage section size, and room temperature tensile tests were conducted at a strain rate of 5.2×10^{-4} s^{-1} by a universal testing machine (model; 8862, Instron Corp., Canton, MA, USA) with a capacity of 10,000 kg.

A compact tension (CT) type loading stage was installed inside an SEM, on which a thin CT specimen with a thickness of 0.5 mm in the grooved section was placed to conduct the *in situ* SEM fracture test.[17–19] A sharp notch with a radius of about 30 to 40 μm was introduced by an electric discharge machine, considering the difficulty to introduce a fatigue crack due to the brittle nature of the amorphous composite.[30,31] Since the CT specimen was very small, the conventional method for measuring the crack size was not available. Thus, the crack size was measured while observing the specimen surface displayed on an SEM screen and momentarily stopping the crack propagation. The load applied to the specimen was continuously measured by a small-scale load cell (maximum load; 50 kg) installed in the stage, and was recorded on an X–Y recorder to obtain the load–time curve. The stress intensity factor was also measured at each crack stopping moment using the measured crack length and load, together with equations conventionally used for CT specimen.

III. RESULTS

A. *Microstructure and Tensile Properties*

The results of our experiments are as follows. EBSD inverse pole figure (IPF) and phase color maps of a Ti-based amorphous composite [composition; $Ti_{53.9}Zr_{30}V_{9.9}Ni_{3.5}Al_{0.9}Be_{1.8}$ (at. pct)] are shown in Figures 1(a) and (b). Dendrites surrounded by boundaries having different orientations of 15 deg or higher are generally considered to be effective dendrites (Figure 1(a)).[14–16] Dendritic structures of β-Ti phase are homogeneously distributed in the amorphous matrix (Figure 1(b)). The average volume fraction and size of effective β dendrites are 74 pct and 81 μm, respectively.[29]

The yield strength, tensile strength, and elongation measured from the room temperature tensile test are 1443, 1511 MPa, and 5.2 pct, respectively.[29] An SEM fractograph of a tensile specimen is shown in Figure 2. The tensile fracture surface contains ductile dimples, cleavage-like facets, and vein patterns. Inside cleavage-like facets, lamellar patterns composed of many parallel lines are shown. Since these patterns are not reported previously, they are called to be 'lamellar cleavage patterns' from now on. Lamellar cleavage patterns and vein patterns are originated from dendrite and amorphous matrix areas, respectively, as confirmed by energy-dispersive spectroscopy (EDS) analysis. Here in EDS analysis, most of V is included in β-Ti dendrites because V is a typical β-Ti stabilizer. Using this considerable difference in V content, dendrite and amorphous matrix areas can be differentiated. The spacing of lamellar cleavage patterns is almost same at 3 to 5 μm.

B. *In Situ SEM Fracture Test*

In order to understand complicated fracture modes occurring on the tensile fracture surface, the detailed fractographic analysis is essentially needed. Since the tensile fractographic results generally give overall information on fracture modes as the tensile load is consistently applied in vertical to the fracture surface,[32,33] the tensile test is not desirable for investigating fracture mechanisms varied with crack propagation speed or stress loading direction. In the present study, thus, the *in situ* SEM fracture test was conducted using CT specimens, and fracture processes as well as fracture modes were observed in detail. In fact, since the CT specimen having a crack or a notch is fractured mostly by the crack initiation and propagation processes, the *in situ* SEM fracture test is favorably applicable to fracture mechanism study of fracture modes varied with crack growth.[17–19] Also, the test results can be well quantified by stress intensity factors at each crack growth stage. The *in situ* SEM fracture test and the detailed fractographic analysis might give a meaningful interpretation of various fracture modes including lamellar cleavage patterns.

Figures 3(a) through (d) are SEM micrographs serially showing fracture processes. When a load is applied (stress intensity factor, K_I = 36 MPa$\sqrt{m}$), a microcrack initiates at the amorphous matrix of the notch tip as marked by an arrow in Figure 3(a). Under a high stress intensity factor (K_I = 39 MPa$\sqrt{m}$), the microcrack propagates mostly along the amorphous matrix at the notch tip to form a longer crack, while dendrites are not deformed (Figure 3b). With the increased stress intensity factor of 40 MPa$\sqrt{m}$, the crack propagates and then stops to be somewhat blunted when the crack meets with a dendrite as marked by arrows in Figure 3(c). Under the higher stress intensity factor of 41 MPa$\sqrt{m}$, the stopped crack rapidly propagates through the CT specimen without any more stopping or blunting (Figure 3d). The overall crack propagation path has a linear pattern with some fluctuations.

Figure 4 shows an R-curve obtained by plotting both crack growth length and apparent stress intensity factor measured during the *in situ* SEM fracture test. Apparent stress intensity factors do not satisfy the plane strain condition because of the introduction of a sharp notch

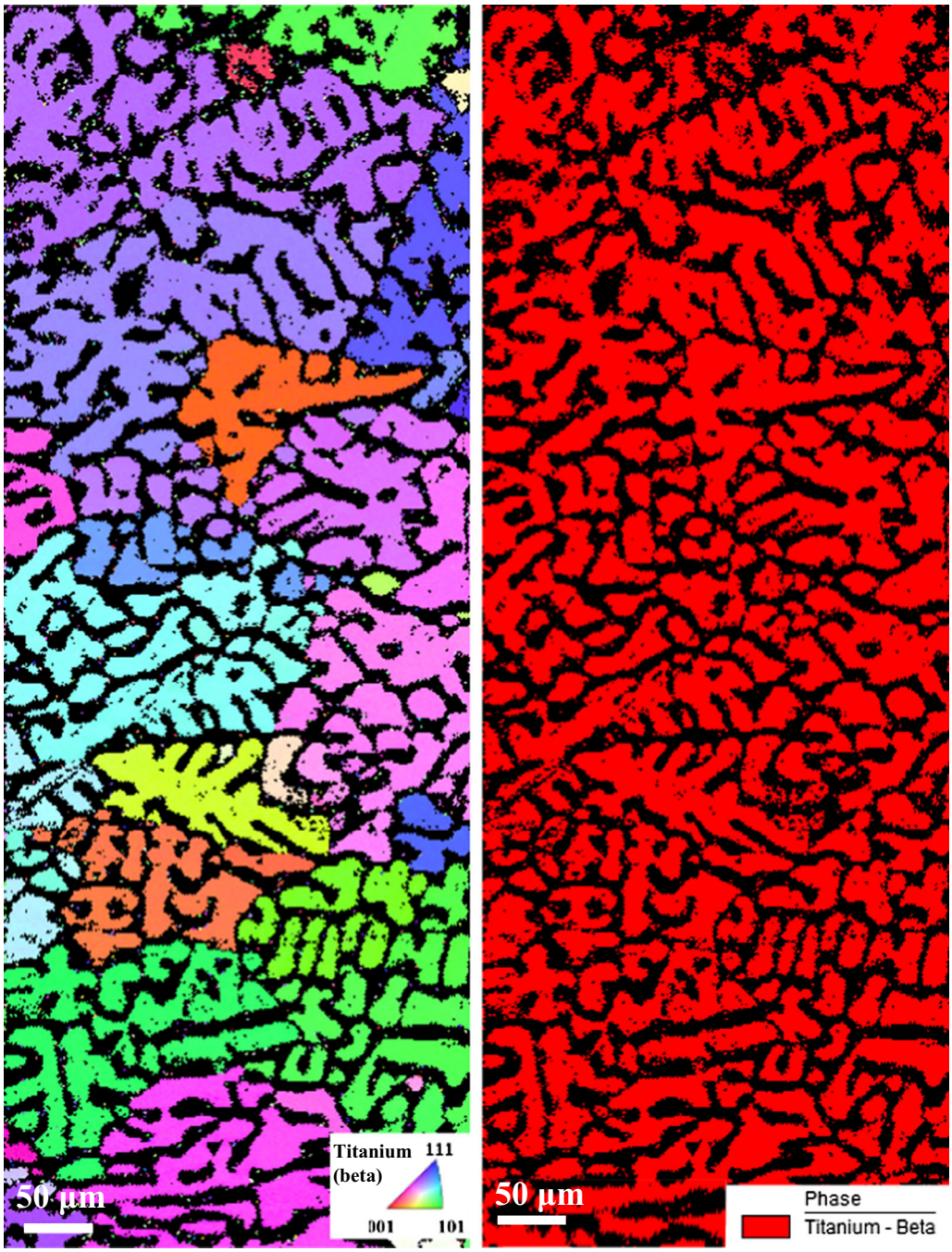

Fig. 1—(*a*) EBSD inverse pole figure (IPF) color map and (*b*) phase color map of the Ti-based amorphous matrix composite. The effective dendrite size measured from the IPF map is 81 μm (Color figure online).

(notch tip radius: about 30 to 40 μm) into a thin CT specimen (thickness; 0.5 mm), instead of a fatigue crack.[30,31] The apparent stress intensity factor at the time of crack initiation is 36 MPa$\sqrt{m}$, but steadily increases up to 41 MPa$\sqrt{m}$ with increasing crack length, which shows the typical R-curve behavior. This R-curve behavior is attributed to the continuous deformation at the crack tip region as dendrites block the crack propagation. Since the crack initiation and propagation processes mainly depend on the resistance to crack growth, the crack growth rate is changed along the crack propagation path (Figures 3(a) through (d)), but its measurement is quite difficult. The crack growth rate is estimated indirectly by assuming that it is varied with the change in crack length and, in more specifically, the slope of stress intensity factor divided by crack growth length. If the slope is almost nil, the resistance to crack growth is almost disappeared, and the crack growth rate is very rapid. Considering that the slope reasonably works as a measure of crack growth rate as well as

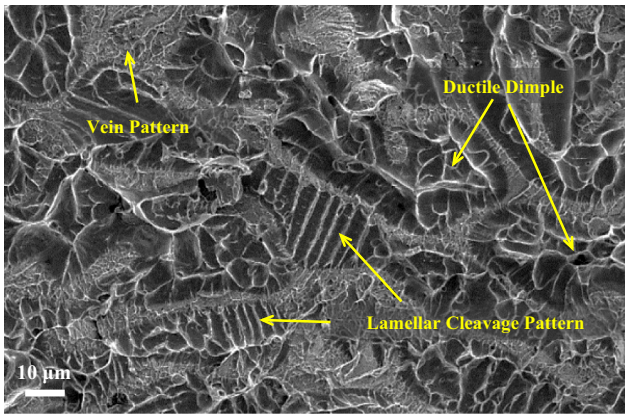

Fig. 2—SEM fractograph of a tensile specimen of the Ti-based amorphous matrix composite. The tensile fracture surface contains ductile dimples, lamellar cleavage patterns, and vein patterns.

resistance to crack growth, the crack growth rates are roughly classified into slow, intermediate, and rapid stages by the slope, as indicated by light-red areas in Figure 4. The slope is 6.2×10^4 MPa/√m in the slow stage, and decreases to 2.3×10^4 MPa/√m and about nil in the intermediate and rapid stages, respectively. The slow stage has the highest slope.

SEM fractographs of the thin CT specimen are shown in Figures 5(a) through (d). In the slow crack growth stage near the notch tip region, ductile dimples, lamellar cleavage patterns, and vein patterns are mixed together as marked by arrows in Figure 5(a), like in the tensile fracture surface (Figure 2), although ductile dimples are not well developed. The spacing of lamellar cleavage patterns is 3 to 5 μm, which is almost same to that of the tensile fracture surface. In the intermediate crack growth stage, the lamellar cleavage pattern mode prevails in dendrite areas, whereas dimples are not found (Figure 5(b)). The spacing of lamellar cleavage patterns is reduced to about 2 μm. Lamellar cleavage patterns are parallel inside some dendrite areas, and the other lamellar patterns are vertically formed. In amorphous matrix areas, both vein patterns and smooth patterns are found. Smooth patterns can be recognized to be a more brittle fracture mode than vein patterns because of their flat and smooth shape.[34,35] When the crack growth rate becomes faster in the rapid crack growth stage, lamellar cleavage patterns and ordinary cleavage facets are observed in dendrite areas, while only smooth patterns are found without vein patterns in amorphous matrix areas (Figure 5(c)). When these cleavage facets are observed in a high-magnification micrograph (Figure 5(d)), they are composed of somewhat flat and smooth surfaces containing many weak river patterns, which give a sign of the decreased fracture resistance.[36]

IV. DISCUSSION

It is interesting to note from the above fractographic results (Figures 5(a) through (d)) that the fracture mode

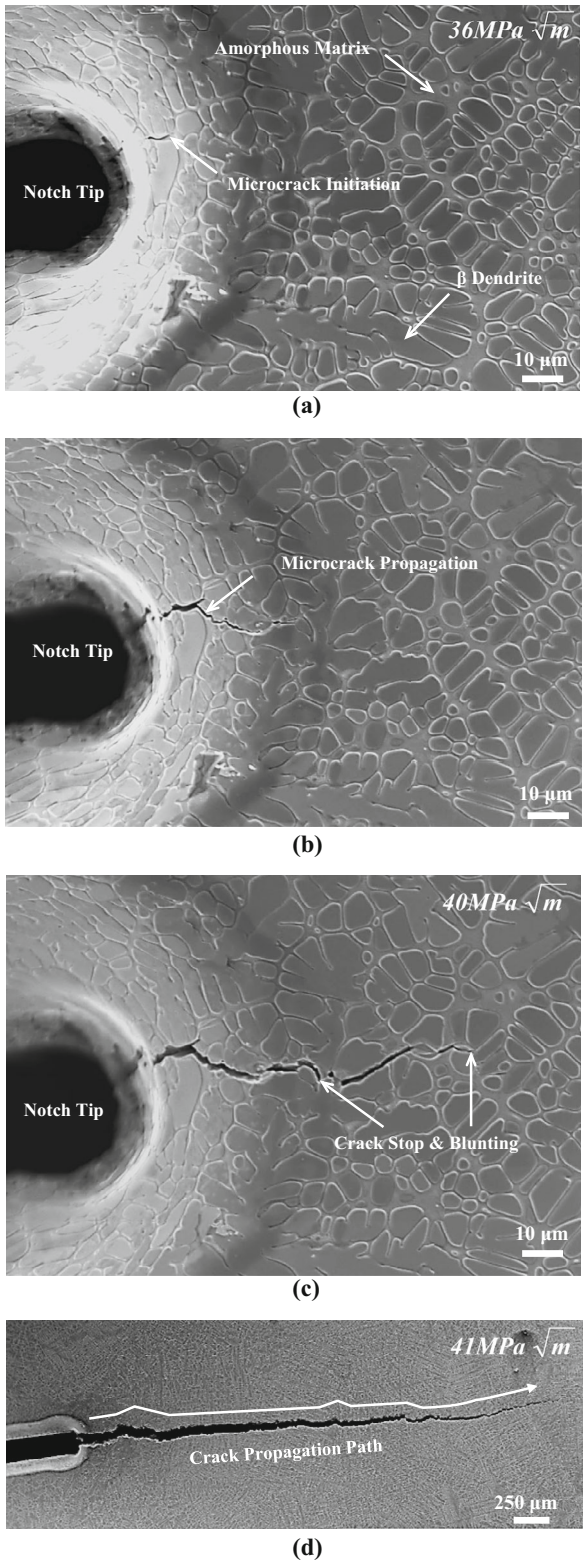

Fig. 3—Direct observation of crack initiation and propagation process. A series of SEM micrographs near a notch tip, showing (*a*) microcrack initiation at the amorphous matrix near the notch tip (K_I = 36 MPa√m), (*b*) microcrack propagation along the amorphous matrix (K_I = 39 MPa√m), (*c*) stop of crack propagation at dendrites and crack blunting (K_I = 40 MPa√m), and (*d*) final crack propagation path (K_I = 41 MPa√m).

becomes brittle as the crack growth rate increases. These results can be reasonably accepted because the time for effectively stopping or blocking the crack growth is not enough, which leads to the reduction in resistance to crack growth. The area fractions of ductile dimpled fracture, lamellar cleavage pattern, and ordinary cleavage fracture observed in dendrite areas and vein pattern and smooth pattern observed in amorphous matrix areas were measured in each crack growth stage, and the results are summarized in Table I. It is noted again that the fracture mode changes from the ductile mode to the brittle mode in both dendrite and amorphous matrix areas.

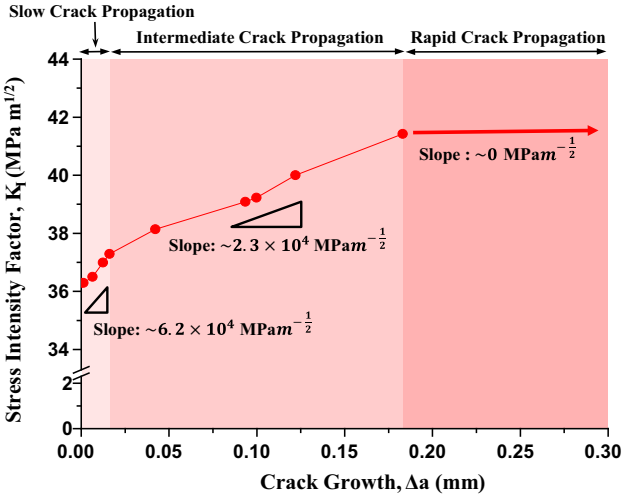

Fig. 4—R-curve obtained by plotting both crack growth length and apparent stress intensity factor measured during the *in situ* SEM fracture test. The crack growth rates are classified by slow, intermediate, and rapid stages, as indicated by light-red areas.

The unique appearance of lamellar cleavage patterns in dendrite areas might be attributed to the step-like cleavage on {100} cleavage planes of β dendrites (bcc structure). When the applied stress direction is momentarily deviated from {100} planes in bcc materials under some brittle fracture environments such as rapid crack growth or low temperature, the propagating crack on {100} planes can stop and turn its direction to another direction.[37] If this crack stopping-turning-returning process is repeated on {100} planes, a step-like cleavage mode can be produced. According to Schultz *et al.*,[37] when the same load is applied on two {100} planes which are vertical to each other in a CaF_2 single crystal, the cleavage crack propagates on these two planes in a zig-zag mode to form step-like patterns.[37] This explanation on step-like cleavage mode in the CaF_2 single crystal cannot be directly applied to the presence of lamellar cleavage patterns in dendrite areas because

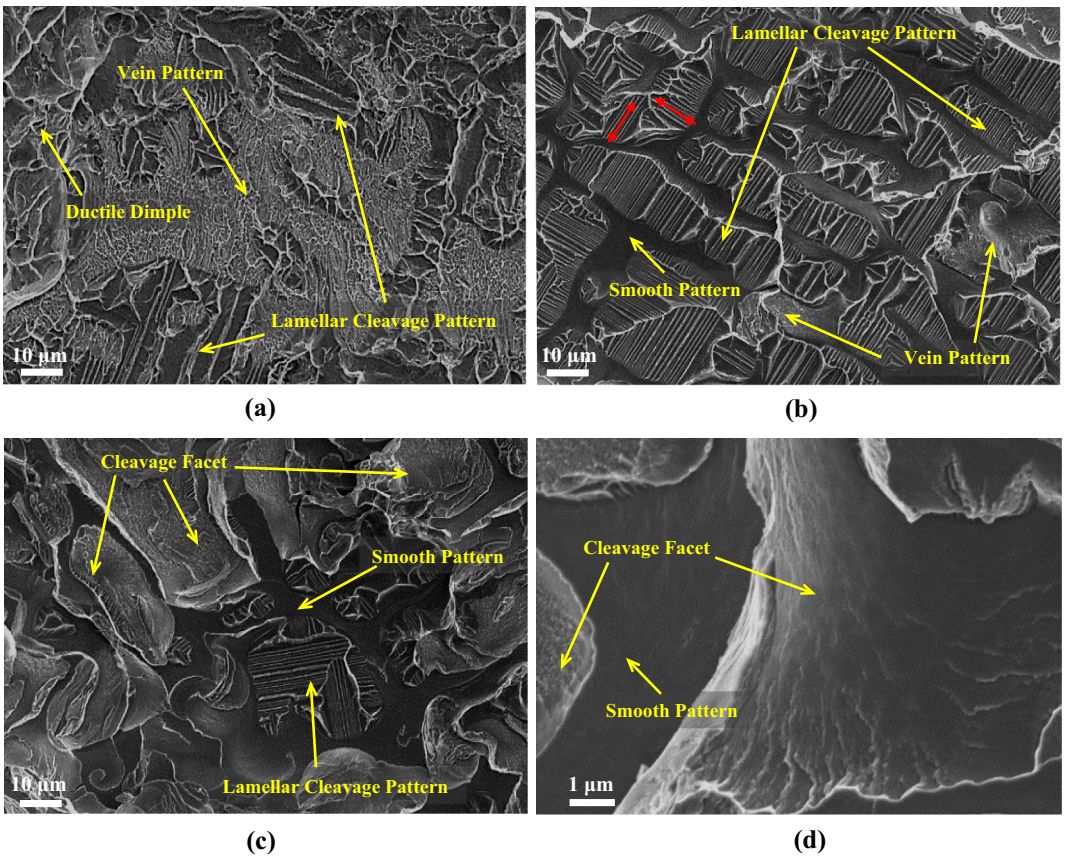

Fig. 5—SEM fractographs of the thin compact tension specimen in the (*a*) slow, (*b*) intermediate, and (*c*), (*d*) rapid crack growth stages, showing ductile dimples, lamellar cleavage patterns, and ordinary cleavage facets originated from dendrite areas, and vein patterns and smooth patterns originated from amorphous matrix areas.

Table I. Area Fractions of Ductile Dimpled Fracture, Lamellar Cleavage Pattern, and ordinary Cleavage Fracture Observed in Dendrite Areas and Vein Pattern and Smooth Pattern Observed in Amorphous Matrix Areas in the Slow, Intermediate, and Rapid Crack Growth Stages. (Unit: Pct)

	Ductile Dendrite			Amorphous Matrix	
Crack Growth Stage	Ductile Dimpled Fracture	Lamellar Cleavage Pattern	Ordinary Cleavage Fracture	Vein Pattern	Smooth Pattern
Slow	12 ± 1.3	57 ± 8.3	—	31 ± 7.6	—
Intermediate	—	67 ± 4.5	—	7 ± 1.5	26 ± 6
Rapid	—	20 ± 2.8	61 ± 7.3	—	19 ± 4.5

most of the lamellar patterns have the same orientation inside one effective dendrite having the same orientation, and their spacing is almost same on each lamellar cleavage facet (Figure 5(b)). Thus, the detailed analyses on how lamellar cleavage patterns are formed by cleavage mechanisms occurring on {100} planes in bcc materials are essentially needed.

In order to examine orientations and planes of lamellar cleavage patterns as well as β dendrites, two dendrite areas containing lamellar cleavage patterns and ductile dimples on tensile fracture surfaces (red-lined rectangular areas in Figures 6(a) and (b)) are analyzed by the EBSD using a field emission scanning electron microscope (FE-SEM) attached with a focused ion beam (FIB, model; Quanta 3D, FEI, Netherlands) equipment. Thick foil specimens including red-lined rectangular areas (width; 2 μm) were prepared by Pt deposition for protecting the surface followed by the ion milling of the exterior side regions (at a voltage of 30 kV and a current of 0.3 nA), as shown in Figure 6(c). Lateral surfaces of the thick foil specimens containing lamellar cleavage patterns and ductile dimples are shown in Figures 6(d) and (e), respectively. The surface profile of lamellar cleavage patterns is composed of many small peaks on a relatively flat base plane (Figure 6(d)). These peaks have 3-dimensional shapes of ridges and valleys. The spacing and height of lamellar pattern peaks are measured to be 1 to 3 μm and 200 to 850 nm, respectively. On the other hand, the surface profile of ductile dimples shows an irregularly curved line without any specific base planes (Figure 6(e)).

The EBSD analysis was conducted on the lateral area (yellow-lined rectangular area in Figure 7(a)) just beneath the lamellar cleavage fracture surface (red-lined area), and IPF map, {001} pole figure, {110} pole figure, and crystallographic orientations are shown in Figures 7(b) through (e). According to the pole figure data, average Euler angle (Bunge) of β dendrite (yellow-lined rectangular area) is (261.6, 13.7, 100.9), as shown in Figure 7(e). This Euler angle indicates that the fracture surface (red-lined area) is parallel with a (100) plane, which matches with one of typical {100} cleavage planes. Since {100} planes have the lowest packing density and the widest planar spacing in bcc materials, they act as typical cleavage facture planes.[38] In addition, the direction of lamellar patterns denoted by a green arrow in Figure 6(a) is parallel with [001] (green arrow mark in Figure 7(e)), while another direction of lamellar patterns denoted by a blue arrow in Figure 6(a) is parallel with [010] (blue arrow mark in Figure 7(e)). This implies that lamellar patterns are formed along different vertical directions, depending on ⟨001⟩ directions acting on the {100} planes. In fact, they often have two different vertical orientations even inside one effective dendrite having the same orientation (Figure 1(a)), as shown by red arrows in Figure 5(b). Figure 7(f) shows a schematic diagram of lamellar cleavage patterns, together with the profile of the fracture surface (red-lined area in Figure 7(a)). Here, the pink-colored plane is a (100) plane which is shown to be relatively flat on the fracture surface, and the green- and blue-colored planes are (110) and (1−10) planes, respectively, which are vertically placed. These (110) and (1−10) planes make ridges and valleys in a 3-dimensional view, and their intersections form ridge lines.

The EBSD analysis was also conducted on the lateral area (yellow-lined rectangular area in Figure 8(a)) just beneath the ductile dimpled fracture surface (red-lined area) as shown in Figures 8(b) through (e). According to the pole figure data, average Euler angle (Bunge) of β dendrite is (297.3, 44.2, 69.0), as shown in Figure 8(e). This indicates that the ductile dimpled fracture surface is not parallel with a (100) plane because the [001] direction is deviated by 35 deg to 45 deg at least from the tensile loading direction as indicated by a curved arrow in Figure 8(c). The plane of the ductile dimpled fracture surface is estimated to be (−413) by an EBSD OIM software as indicated by a pink-colored plane in Figure 8(e). When the ductile dimpled fracture surface is not vertical to the tensile loading direction, like in the case of Figure 8(e), the externally applied tensile stress is divided into normal and shear stresses. Thus, the normal stress acting on the (100) plane is quite low, unlike in the case of the lamellar cleavage facet, thereby leading to the formation of ductile dimpled fracture instead of lamellar cleavage fracture. This result indicates that the ductile dimpled fracture or lamellar cleavage fracture can occur even in one dendrite, depending on the deviation between ⟨001⟩ directions of {100} planes and tensile loading direction acting on the {100} planes.

It is confirmed from the EBSD analysis data of the tensile fracture surface that the lamellar cleavage fracture is one kind of cleavage fracture modes occurring in bcc materials, although lamellar cleavage patterns are spaced in an almost same interval and are vertically placed inside dendrites. In addition, the appearance of ductile dimpled fracture or lamellar cleavage fracture depends mainly on the orientation difference between the orientation of

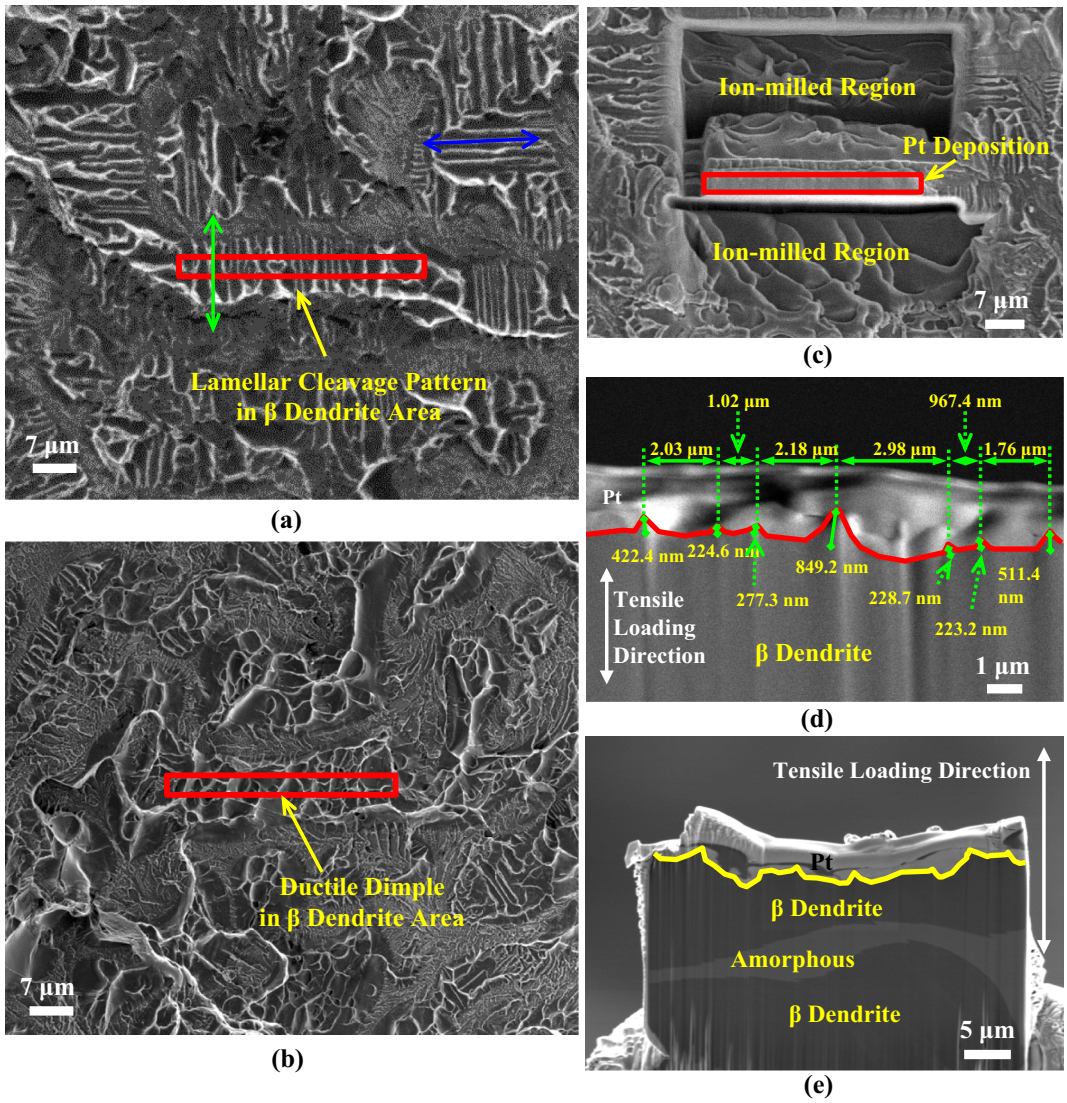

Fig. 6—Preparation of thick foil specimen for EBSD analysis. SEM fractographs of the tensile specimen, showing (*a*) lamellar cleavage patterns, (*b*) ductile dimples, and (*c*) thick foil specimen including red-lined rectangular area in a. A thick foil specimen was prepared by Pt deposition for protecting the surface followed by the ion milling as shown in c, and was photographed in the 52 deg tilted condition. (*d*, *e*) SEM micrographs of lateral surfaces of the thick foil specimens containing lamellar cleavage patterns and ductile dimples, respectively (Color figure online).

dendrite and tensile loading direction. However, this dependence of fracture mode on orientation difference does not sufficiently explain the fractographic results showing various fracture modes in the CT specimen. This is because the stress distribution at the crack tip and crack growth rate as well as the dendrite orientation and externally loaded stress direction can affect the overall fracture mode. In particular, the crack growth rate importantly influences the fracture mode, and consequently leads to the ductile-to-brittle transition (ductile dimpled fracture → lamellar cleavage fracture → ordinary cleavage fracture) in dendrite areas.

This ductile-to-brittle transition phenomenon occurring even in the same composite by the increase in crack growth rate can be explained by the concept of the time required for the crack growth. In the slow crack growth stage, the crack has enough time to keep away from {100} cleavage planes and to propagate on other planes in a ductile dimpled mode. When the crack growth rate increases, the time for finding other planes except {100} may become insufficient. In this case, the crack propagates along a (100) cleavage plane, but its propagation plane can be changed to one of {110} planes which are tilted by 45 deg with the (100) plane. If this crack propagation proceeds repeatedly on {100} and {110} planes, as shown in Figure 7(f), lamellar cleavage patterns can be produced on a flat base plane of {100} planes. When the crack growth becomes fast further, the crack propagates in an ordinary cleavage mode on {100} planes without producing lamellar cleavage patterns. In amorphous matrix areas, vein patterns are formed in the slow crack growth stage, but are changed to smooth patterns, whose resistance to crack propagation hardly exists, because the time for forming vein patterns is not enough. Therefore, the crack growth rate acts as a major parameter affecting the ductile-to-brittle transition of fracture mode.

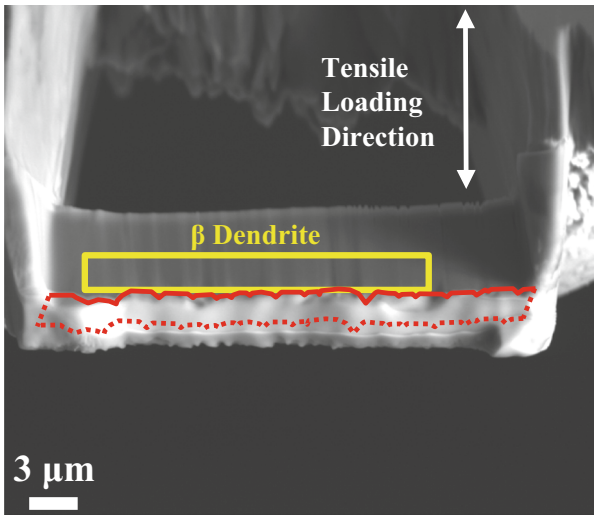

(a)

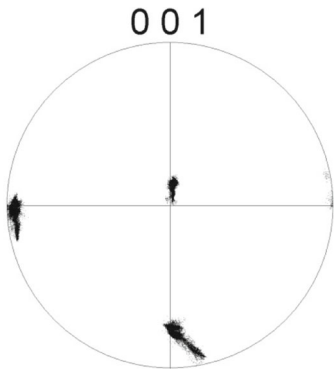

(c)

(b)

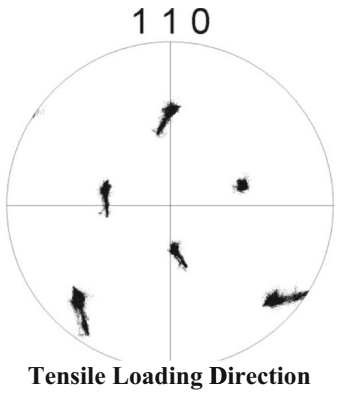

(d)

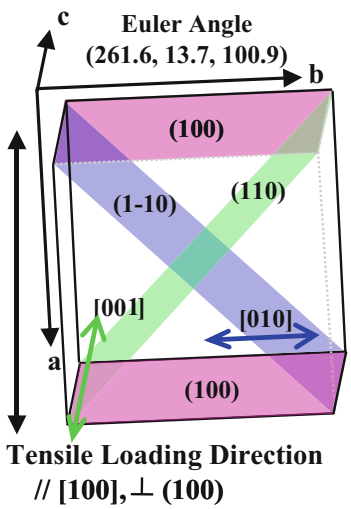

(e)

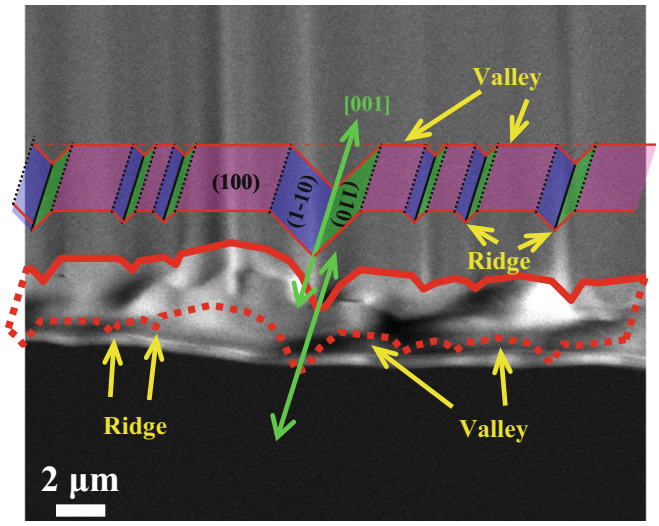

(f)

Fig. 7—Formation mechanism of lamellar cleavage patterns. (*a*) SEM micrograph of the thick foil specimen (in the 70 deg tilted condition), (*b*) EBSD IPF map, (*c*) {001} pole figure, (*d*) {110} pole figure, and (*e*) average Euler orientations of the lateral area (yellow-lined rectangular area in a) just beneath the lamellar cleavage facet (red-lined area in a). (*f*) Shows a schematic diagram of lamellar cleavage patterns, together with the profile of the fracture surface [red-lined area in (a)] (Color figure online).

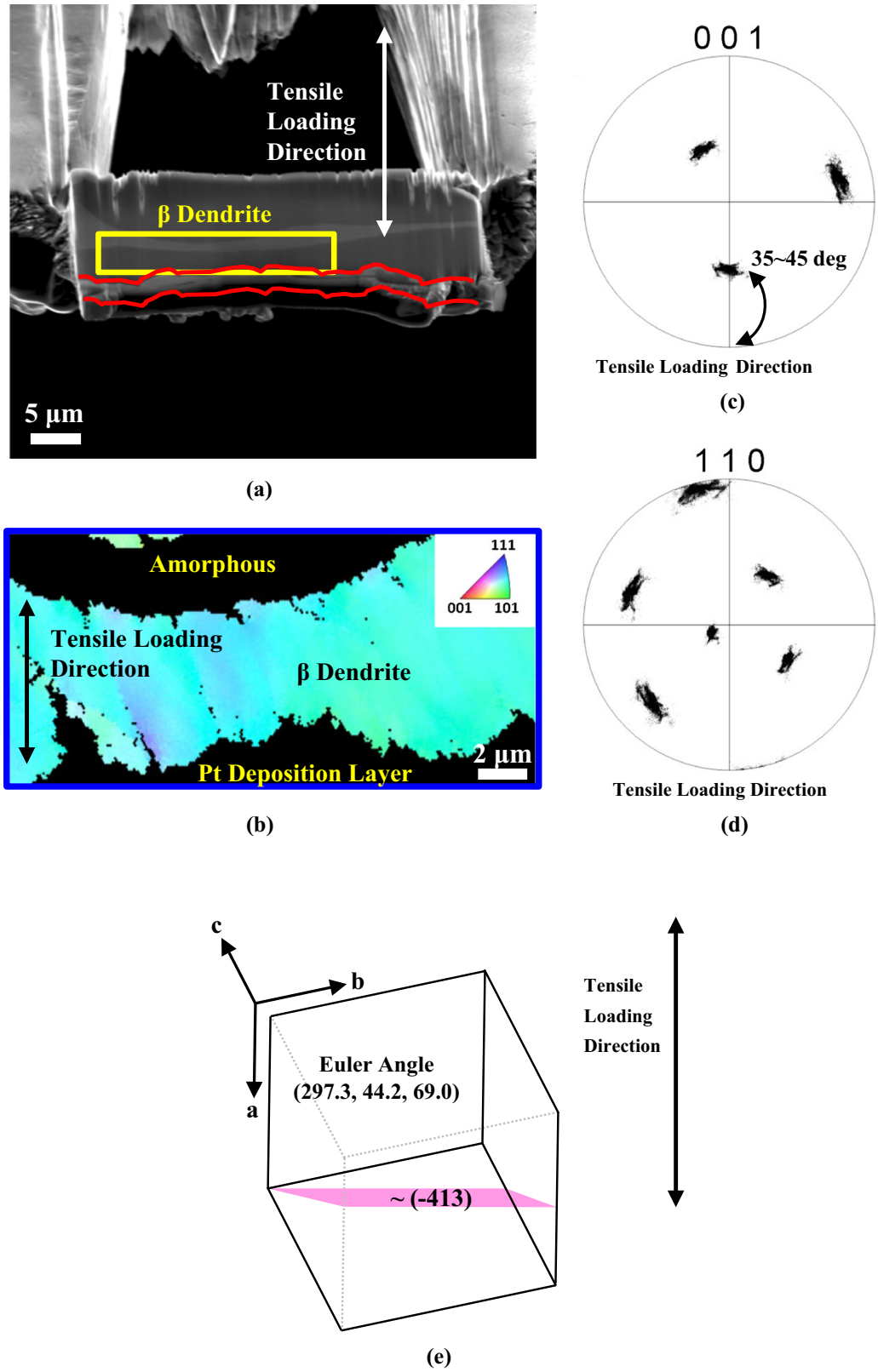

Fig. 8—Formation mechanism of ductile dimples. (*a*) SEM micrograph of the thick foil specimen (in the 70 deg tilted condition), (*b*) EBSD IPF map, (*c*) (001) pole figure, (*d*) (110) pole figure, and (*e*) crystallographic orientations of the lateral area (yellow-lined rectangular area in a) just beneath the ductile dimpled fracture surface [red-lined area in (a)] (Color figure online).

V. SUMMARY

The detailed fractographic results including the relation between fracture mode, resistance to crack growth, and crack growth rate are valuable for interpreting fracture modes of the present Ti-based amorphous matrix composite. In fact, the lamellar cleavage pattern formed in dendrite areas is a unique fracture mode, which has not been reported in previous studies on amorphous alloys or composites and conventional metals or alloys. It is confirmed from the EBSD analysis that the appearance of lamellar cleavage pattern is a kind of cleavage mode occurring when the crack propagation on {100} planes is repeatedly interrupted by the difference between dendrite orientation and loading direction. Furthermore, it is a meaningful result that the ductile-to-brittle transition of fracture mode in dendrite areas is influenced by dendrite orientation as well as crack growth rate.

ACKNOWLEDGMENTS

This work was supported by the National Research Foundation of Korea (NRF) Grant (No. 2010-0026981) funded by the Ministry of Education, Science, and Technology, Korea.

REFERENCES

1. W. Chen, Y. Wang, J. Qiang, and V. Dong: *Acta Mater*., 2003, vol. 51, pp. 1899–07.
2. A. Inoue: *Acta Mater*., 2000, vol. 48, pp. 279–06.
3. H.A. Shivaee, A. Castellero, P. Rizzi, P. Tiberto, H.R.M. Hosseini, and M. Baricco: *Met. Mater. Int*., 2013, vol. 19, pp. 643–49.
4. R. Busch, A. Masuhr, and W.L. Johnson: *Mater. Sci. Eng. A*, 2001, vols. 304–306, pp. 97–102.
5. G. Duan, A. Wiest, M.L. Lind, A. Kahl, and W.L. Johnson: *Scripta Mater*., 2008, vol. 58, pp. 465–68.
6. M. Taboosi, F. Karimzadeh, M.H. Enayati, S. Lee, and H.S. Kim: *Met. Mater. Int*., 2013, vol. 19, pp. 901–06.
7. H.-K. Kim, M. Lee, K.-R. Lee, and J.-C. Lee: *Acta Mater*., 2013, vol. 61, pp. 6597–08.
8. D.E. Polk and D. Turnbull: *Acta Metall*., 1972, vol. 20, pp. 493–98.
9. C.A. Pampillow: *Scripta Metall*., 1972, vol. 6, pp. 915–17.
10. C.C. Hays, C.P. Kim, and W.L. Johnson: *Phys. Rev. Lett*., 2000, vol. 84, pp. 2901–04.
11. T.E. Kim, S.W. Sohn, J.M. Park, C.W. Bang, W.T. Kim, and D.H. Kim: *Met. Mater. Int*., 2013, vol. 19, pp. 667–71.
12. C.C. Hays, W.L. Johnson, and C.P. Kim: *Mater. Sci. Eng. A*, 2001, vols. 304–306, pp. 650–55.
13. D.C. Hofmann, J.-Y. Suh, A. Wiest, G. Duan, M.L. Lind, M.D. Demetriou, and W.L. Johnson: *Nature*, 2008, vol. 451, pp. 1085–89.
14. Y.S. Oh, C.P. Kim, S. Lee, and N.J. Kim: *Acta Mater*., 2011, vol. 59, pp. 7277–86.
15. D.J. Ha, C.P. Kim, and S. Lee: *Mater. Sci. Eng. A*, 2012, vol. 552, pp. 404–09.
16. D.J. Ha, C.P. Kim, and S. Lee: *Mater. Sci. Eng. A*, 2012, vol. 558, pp. 558–65.
17. J.G. Lee, D.-G. Lee, S. Lee, and N.J. Kim: *Metall. Mater. Trans. A*, 2004, vol. 35A, pp. 3753–61.
18. J.G. Lee, K.-S. Sohn, S. Lee, N.J. Kim, and C.P. Kim: *Mater. Sci. Eng. A*, 2007, vol. 464, pp. 261–68.
19. C. Jeon, C.P. Kim, and S. Lee: *Metall. Mater. Trans. A*, 2012, vol. 43A, pp. 3675–3686.
20. M.W. Lee, H.J. Shin, S.H. Hong, J.T. Kim, H. Choi-Yim, Y. Seo, W.H. Lee, P. Yu, M. Qian, J.K. Lee, and K.B. Kim: *Met. Mater. Int*., 2014, vol. 20, pp. 1–5.
21. D.L. Davison: *Metall. Trans. A*, 1987, vol. 18, pp. 2115–28.
22. S.R. Nutt and L.M. Duva: *Scripta Metall*., 1986, vol. 20, pp. 1055–58.
23. J.P. Escobedo and Y.M. Gupta: *J. Appl. Phys*., 2010, vol. 107, pp. 125302-1–125302-9.
24. P. Murali, T.F. Guo, Y.W. Zhang, R. Narasimhan, Y. Li, and H.J. Gao: *Phys. Rev. Lett*., 2011, vol. 107, pp. 215501-1–215501-5.
25. Z.F. Zhang, G. He, J. Eckert, and L. Schultz: *Phys. Rev. Lett*., 2003, vol. 91, pp. 045505-1–045505-4.
26. C. John: *Phil. Mag*., 1975, vol. 32, pp. 1193–12.
27. H. Li and F. Ebrahimi: *Adv. Mater*., 2005, vol. 17, pp. 1969–72.
28. E.M. Schulson and D.R. Barker: *Scripta Metall*., 1983, vol. 17, pp. 519–22.
29. C. Jeon, C.P. Kim, S.-H. Joo, H.S. Kim, and S. Lee: *Acta Mater*., 2013, vol. 61, pp. 3012–26.
30. Kishore, S. Shankar, and S. Sankaran: *Mater. Sci. Eng. A*, 2005, vol. 412, pp. 153–58.
31. S.G. Lee, G.R. Patel, A.M. Gokhale, A. Sreeranganathan, and M.F. Horstemeyer: *Mater. Sci. Eng. A*, 2006, vol. 427, pp. 255–62.
32. R.O. Ritchie and R.M. Horn: *Metall. Trans. A*, 1978, vol. 9, pp. 331–41.
33. Y.-H. Kim, D. Kwon, and S. Lee: *Acta Metall*., 1997, vol. 42, pp. 1887–91.
34. M. Kusy, U. Kühn, A. Concustell, A. Gebert, J. Das, J. Eckert, L. Schultz, and M.D. Baro: *Intermetallics*, 2006, vol. 14, pp. 982–86.
35. Y. Huang, D. Wang, Z. Shang, and J. Shen: *J. Alloys Compd*., 2012, vol. 541, pp. 359–64.
36. J.R. Tarpani, M.H.P. Braz, W.W.B. Filho, and D. Spinelli: *Mater. Res*., 2002, vol. 5, pp. 357–64.
37. R.A. Schultz, M.C. Jensen, and R.C. Bradt: *Int. J. Fract*., 1994, vol. 65, pp. 291–12.
38. T.L. Anderson: *Fracture Mechanics*, 3rd ed., Taylor & Francis Group, New York, 2005, pp. 234–44.